Reversible catastrophic oxidation of a 38Fe-34Ni-25Cr alloy induced by sodium sulphate at low oxygen potential atmospheres

L. Couture, Francois Ropital, F. Grosjean, Jean Kittel, V. Parry, Y. Wouters

▶ **To cite this version:**

L. Couture, Francois Ropital, F. Grosjean, Jean Kittel, V. Parry, et al.. Reversible catastrophic oxidation of a 38Fe-34Ni-25Cr alloy induced by sodium sulphate at low oxygen potential atmospheres. Corrosion Science, 2012, 55, pp.133-139. 10.1016/j.corsci.2011.10.010 . hal-00674978

HAL Id: hal-00674978
https://hal.science/hal-00674978

Submitted on 20 Dec 2019

HAL is a multi-disciplinary open access archive for the deposit and dissemination of scientific research documents, whether they are published or not. The documents may come from teaching and research institutions in France or abroad, or from public or private research centers.

L'archive ouverte pluridisciplinaire **HAL**, est destinée au dépôt et à la diffusion de documents scientifiques de niveau recherche, publiés ou non, émanant des établissements d'enseignement et de recherche français ou étrangers, des laboratoires publics ou privés.

Reversible catastrophic oxidation of a 38Fe-34Ni-25Cr alloy induced by sodium sulphate at low oxygen potential atmospheres

L. Couture[1,2], F. Ropital[2], F. Grosjean[2], J. Kittel[2], V. Parry[1], Y. Wouters[1]

[1]*SIMaP, Grenoble-INP / UJF / CNRS, BP 75, 38402 Saint Martin d'Hères cedex, France*

[2]*IFP Énergies Nouvelles, Rond Point de l'échangeur de Solaize BP3, 69360 Solaize, France*

Abstract

The chromia-forming nickel-based alloy Haynes® HR-120 was oxidised with and without Na_2SO_4 deposit in a $CO/H_2/CO_2$ (45/45/10 %vol.) simulated process atmosphere at 900°C for 96 hours. During the first hours of oxidation, samples covered by sodium sulphate exhibit higher oxidation rate than non-covered ones. However, after 24 hours both sulphate-covered and uncovered specimens follow the same linear kinetics. In this very low oxygen partial pressure environment (10^{-18} atm), the presence of Na_2SO_4 promotes the growth of localized iron-rich oxide nodules leading to the observed accelerated oxidation. The development of these nodules is discussed to be the result of the chromia dissolution induced by a basic fluxing mechanism. As soon as the salt is evaporated, slower kinetics are observed and the nodules disappear. In these specific conditions, the oxidation could be considered as a self-healing process.

Keywords:

C. Catastrophic oxidation, C. hot corrosion, A. Na_2SO_4, C. low oxygen partial pressure.

1 Introduction

One key factor in ensuring the success of biofuel technologies is the availability of biomass resources. The targets set in France and Europe for the replacement of oil products in the transportation sector by 2010 can be met by converting farm surpluses into biofuels. In order to increase the production of biofuels, it will be necessary to mobilize resources that are more abundant and potentially less costly, as lignocellulosic materials. The future of biofuels therefore depends on establishing the "second generation" biofuel pathways able to convert lignocellulosic materials into ethanol, biodiesel and biokerosene. The lignocellulosic materials correspond to all products composed of cellulose, hemicelluloses and lignin, as wood or straw. These materials can be converted to a fuel that can replace diesel fuel and kerosene (biomass-to-liquids fuels) or gasoline (ethanol).

In this study, we take an interest at corrosion phenomena that could occur during the thermochemical conversion of biomass to fuel BTL (Biomass To Liquid). One of the thermochemical BTL process includes a gasification step in order to generate the synthetic gas (syngas) which is subsequently transformed into fuels by the Fisher Tropsch process. However, alkaline salts (mainly potassium and sodium sulphates and chlorides) are present in the biomass and can induce detrimental high temperature corrosion of the refractory alloys onto which they may condensate as a liquid phase. In addition to a possible degradation of the exchanger tubes following the gasification reactor, volatile corrosion products can contaminate the syngas and disorder the catalytic activity of the Fisher Tropsch process. In the present work, it has been undertaken a parametric study with the influence of sodium sulphate in direct contact with chromia-forming alloy. The tests are performed at 900°C in a $CO/H_2/CO_2$ (45/45/10 %vol.) atmosphere for durations up to 96 h. The thermodynamic calculations will show in chapter 4.3 that in these conditions sodium sulphate is not stable, meaning that the chosen atmosphere does not actually simulate a biomass gasifier. Nevertheless, the goal of the present work, in a first step, is simply to investigate the effect of sodium sulphate on the high-temperature corrosion.

2 Experimental

2.1 Metallic samples and salt spray procedure

The material used in this study is the austenitic alloy Haynes® HR-120. Its chemical composition is shown in table 1. Specimens of 20 × 10 mm^2 were cut from a 1 mm thick sheet. Specimens were ground from 320 SiC grit to a 1200 SiC grit finish and finally rinsed with distilled water.

Prior to carrying out oxidation runs, the samples were sprayed on all sides with an aqueous saturated solution of Na_2SO_4, leading to the formation of a network of salted drops. After a heating step in a furnace at 150°C during 15 min and cooling to room temperature, localized crystallites appeared on the surface, forming a network of salt rings (Figure 1). The average diameter of the rings is in the range 50-200 µm, the ring surface density is about 1.8 per mm^2 and the average amount of deposited salt is 0.75 $mg*cm^{-2}$.

2.2 Experiments

TGA tests were carried out in a flowing mixture of CO, H_2 and CO_2 respectively 45/45/10 %vol. The samples were heated from room temperature up to 900°C at rate of $20°C*min^{-1}$ under argon in order to avoid any oxidation. The oxidation tests were started when the syngas atmosphere was introduced into the reactor with a flow rate of 100 $mL*min^{-1}$. After 96 h, the reactor was flushed with argon and

the samples were cooled down to room temperature under this atmosphere to avoid any oxidation and coke deposition which is known to occur on iron and nickel oxidised surface under high carbon activity atmospheres [1,2] (Figure 2).

2.3 Analyses

After oxidation, the samples were analyzed by XRD and SEM/EDS analysis. The X-ray diffractograms were obtained using Cu K_α radiation of a Rigaku Miniflex II. Surface and transverse SEM views of the samples and EDS analysis were obtained using a LEO S440 Stereoscan instrument equipped with the EDAX Genesis software.

3 Results

3.1. Sodium sulphate behaviour at high temperatures

To assess the behaviour of sodium sulphate during the high temperature oxidation steps, a mass of 34 mg of commercial Na_2SO_4 was placed in an alumina crucible (height: 6 mm, diameter: 8 mm) and heated to 900°C for 40 h under argon. The same experiment was then performed under the syngas atmosphere. Figure 3 presents the comparative obtained results. Under argon, it appears that the volatilisation of Na_2SO_4 is initially high, near 1.8 $mg*h^{-1}*cm^{-2}$ during the first hour, then decreasing rapidly to a very small near constant value (~ 2.5 $\mu g*h^{-1}*cm^{-2}$). Considering that the melting point of Na_2SO_4 is 884°C, this behaviour corresponds to the rapid initial volatilisation of the fine molten droplets of salt before going to the steady-state volatilisation of the molten bath in the crucible.

Under the syngas atmosphere, the results differ completely, with a very high volatilisation rate (> 25 $mg*h^{-1}*cm^{-2}$) and quite complete disappearance of the condensed phase after a few hours only, showing evidence of chemical interaction between Na_2SO_4 and the syngas, with its transformation into more volatile species.

3.2. Corrosion kinetics

The kinetic impact of Na_2SO_4 towards alloy Haynes HR-120 under the syngas atmosphere is illustrated in Figure 4a, showing the mass gain as a function of exposure time. In the absence of Na_2SO_4, the mass gain follows a linear rate law and remains low, less than 0.2 $mg*cm^{-2}$ after 96 h. Assuming that the chromium oxide is the only constituent of this oxide layer, its thickness at the end of the runs is calculated to be 1.5 µm. On the other hand, the presence of the salt induces a two-stage

corrosion kinetics. Initially, a high rate is observed, with a mass increase of 0.6 mg*cm^{-2} after 12 h, followed by a very slight mass gain in the second stage. Furthermore, due to the rapid volatilisation of the salt, the mass gain measured during the first corrosion stage is obviously under evaluated and the actual mass gain can be potentially much higher. When the oxidation proceeds, the derivative of the mass gain curve display on Figure 4b, indicates that the rate becomes linear and similar to the one recorded without salt.

3.3. Chemical and morphological observations

The surface and cross-section morphologies of the formed scales exhibited marked differences in the two conditions (without and with salt). Figure 5a shows the SEM cross sectional image of uncovered HR-120 after 96 h exposure at 900°C under the syngas atmosphere. The oxide scale seems to be dense, nonporous and protective. The thickness of the oxide scale is in the range of 1 µm. EDX analysis reveals that the scale consists of chromium-rich oxide.

In presence of salt (Figures 5b and 5c), the protective scale is no longer observed but iron-rich nodules with a diameter ranging from 10 to 200 µm have been formed. EDX analysis indicates that they consist of iron and chromium oxide(s). Such typical nodules, result of concomitant internal and external attacks, lead to the loss of the protective character of the scale. Taking into account the size and the surface density of these nodules, it is proposed to associate the sites of their growth with the ones occupied by the salt before oxidation. SEM surface views presented on Figure 6 reveal that the nodules clearly subside with exposition time. After 96 h at 900°C, only nodules that have collapsed are still observed.

Figure 7 presents the X-ray diffraction analysis results of the corrosion products obtained after the exposition of HR-120 to syngas in presence and in absence of salt deposit at 900°C during 96 h.

Diffraction peaks arising from the substrate (γ phase) were observed for both samples. Taking into account the X-Rays depth penetration of several microns, this result is in good agreement with our estimation of oxide scales thicknesses from thermogravimetric analysis.

Without salt, the X-ray diffraction analysis has identified the presence of the rhombohedral oxide solid solution $(Fe_xCr_{1-x})_2O_3$ (R phase) and of the spinel-type oxide $(M_{1-x}Cr_x)_3O_4$ with M = Fe and or Mn (S phase). With sodium sulphate, in addition to the above detected phases, the line at $2\theta = 16.1°$ is seen to be related to sodium chromite $NaCrO_2$ phase (C phase, JCPDS file no. 38-1204). Furthermore, X-ray intensity ratio of R/γ and S/γ phases are higher in presence of salt. This results indicates that the oxide layer is thicker. With the exception of these lines, the spectra of the covered and uncovered samples present a lot of similarity after 96 hours. It seems that the structural

composition of the oxide scale in both conditions is relatively close and consistent with the other observations reported without salt at high oxygen partial pressure [5,6].

X-ray diffraction analysis after oxidation in presence of salt for short periods of time (5, 15 and 60 min) is also presented in Figure 8. All the XRD patterns present lines arising from the substrate, the solid solution $(Fe_xCr_{1-x})_2O_3$ and the spinel $(Cr_xM_{1-x})_3O_4$. In addition, a clear increase of sodium chromite lines with time is observed showing that this compound is probably formed during a short period of oxidation in parallel with the evolution of the nodules.

4 Discussion

4.1. Thermodynamic conditions

From a thermodynamic point of view, the atmosphere used for the experiments does not keep the initial composition 45CO, $45H_2$, $10CO_2$ (% vol.) when heated to high temperatures. As shown in Fig. 9, low temperatures promote the formation of carbon dioxide and water vapour. At 900°C, the temperature of the present experiments, the equilibrium composition of the gas is 50CO, $40H_2$, $5CO_2$, $5H_2O$ (% vol.) with minor CH_4.

In such a reducing atmosphere, the oxygen partial pressure is very low and conversely the carbon activity is equal to one for temperatures lower than 761°C (Fig. 2). Carbon does not deposit during the present isothermal experiments, but care was taken to avoid deposition during heating and cooling steps.

The stable solid compounds in the absence of sodium sulphate are presented in Fig. 10 showing the calculated partial pressure of oxygen versus the reciprocal temperature for the various solid-solid equilibria of the iron-chromium system [FactSage, SGTE 2009].

In the calculations, nickel was omitted for clarity, as nickel oxides are less stable than iron and chromium oxides and do not interfere in the oxidation scales. In this diagram was superimposed the calculated oxygen partial pressure from syngas atmosphere. It appears that chromia is thermodynamically stable in contact with the process atmosphere, together with iron chromite $FeCr_2O_4$, while binary iron oxides are not stable.

Considering now the behaviour of sodium sulphate when heated, the calculations show that this compound is little volatile in vacuum or in inert atmospheres, with the solid-gas equilibrium partial pressure of molecular sulphate lying around 10^{-7} bar at 900°C. Slight decomposition also occurs, mainly giving molecular Na, SO_2 and O_2 with equilibrium pressures in the same range. Other gaseous species are negligible (SO_3 and NaO in the range 10^{-11} – 10^{-12} bar). Using the Hertz-Langmuir relation, the evaporation rate of gaseous sodium sulphate at 900°C in vacuum could be

calculated to be ~ 5 mg*h^{-1}*cm^{-2}, very close to that measured during the first instants. This value corresponds to the maximum possible evaporation rate for this compound. On the other hand, its minimum evaporation rate is achieved in the equilibrium regime, where the gas flux continuously carries the equilibrium amount of vapour. In this situation, the calculated evaporation rate is ~ 1 µg*h^{-1}*cm^{-2}. The measured steady-state evaporation rate of ~ 2.5 µg*h^{-1}*cm^{-2} is therefore very close to this regime, showing low influence of the mass transport in the boundary layer.

In presence of the $CO/H_2/CO_2$ (% vol.) process atmosphere, the situation is completely changed, as sodium sulphate is not stable according to the thermodynamic calculations. Figure 11 shows the equilibrium activity of the major solid and gaseous constituents for an initial large excess of atmosphere compared to solid Na_2SO_4 (molar ratio 10^5:1). The calculations show that, at low temperatures, solid sodium carbonate is stable, but no solid product remains at 800°C and above. Total gaseous sodium (Na + NaOH), hydrogen sulphide and sodium sulphide are the volatile major products. When using a small excess of gas in the calculations (molar ratio 10:1), solid sodium carbonate and/or solid sodium sulphide are stable, with the pressure of hydrogen sulphide reaching 10^{-3} to 10^{-1} bar (Fig. 12). These results show that sodium sulphate is totally vaporised in flowing process atmosphere, but that transient sodium carbonate and/or sulphide can remain solid in slow mass transfer locations.

4.2. Kinetic without salt

Expositions of Haynes HR-120 specimens at 900°C under syngas atmosphere in the absence of Na_2SO_4, exhibits excellent high temperature corrosion resistance, marked by the growth on the alloy surface of a continuous chromium-rich oxide, probably enriched in its upper part with manganese, forming the spinel phase $Mn_xCr_{(3-x)}O_4$. Tan *et al.* [22] showed that the oxidation of austenitic steel exposed under low $P(O_2)$ generate the formation of a thin oxide scale characterized by a very slight mass gain. This observation is widely observed in the literature for whatever atmosphere [23,24]. Lobnig *et al.* [4] report that despite the fact that diffusivity of Cr, Fe and Ni in chromia is within the same order of magnitude, Mn atoms diffusion velocity is 100 times greater than the one of Cr atoms in Cr_2O_3 layers. Thus, $MnCr_2O_4$ spinel is usually present on top of chromia scales due to its high thermodynamic stability and to the quick outward-diffusion of manganese [7,8,23,24]. Moreover, the chemical composition of this oxide layer formed at low oxygen partial pressure is typical to the one observed on other chromium rich nickel base alloys containing a small quantity of manganese exposed to high oxidizing atmospheres [5,6,9,10]. In addition, this scale appears to be protective, according to the low mass gain after 96 h of oxidation. However, the observed linear rate law points out that the oxidation is probably limited by a surface reaction, contrary to what happens in high

P(O_2) atmospheres, where chromium diffusion through the oxide scale is the rate-limiting process, inducing parabolic kinetics. In the present case, the oxidising molecules H_2O and CO_2 need to be decomposed in the chemisorbed state before oxygen may be available for entering the oxide scale. According to available data, the linear rate determined in the present work is in the range of those measured for chromia growth on chromium in water vapour (10^{-4} mg*h^{-1}*cm^{-2} at 800°C [11]) or on AISI441 stainless steel in CO_2 (9.10^{-3} mg*h^{-1}*cm^{-2} at 900°C [12]).

4.3. Kinetic in presence of salt

However, the presence of Na_2SO_4 is quite corrosive towards Haynes HR-120. According to the above-described observations, a localised fast growing oxide can be formed through direct contact with Na_2SO_4. The development of such iron-rich nodules combined to an important mass gain during the 12 first hours is the classical signature of catastrophic oxidation. Regarding the thermodynamic calculations here above, sodium sulphate is not stable in the present temperature and atmosphere conditions.

Stability of sodium sulphate can be illustrated through a stability diagramm Na-O-S. Such a diagram is shown in Figure 13, where the activities of O_2 and SO_3 are used as coordinates. Dioxygen and sulfur trioxide partial pressure in syngas atmosphere are plotted by a circle filled. According to Kofstad, the activity of SO_3 can alternatively be expressed in terms of the activity of Na_2O, as the equilibrium of the reaction **(1)** :

$$Na_2SO_4 \rightleftharpoons Na_2O + SO_3 \quad \textbf{(1)}$$

can be expressed by the reaction **(2)**

$$a_{Na_2O}\, a_{SO_3} \rightleftharpoons \text{constant} \times a_{Na_2SO_4} \quad \textbf{(2)}$$

For pure Na_2SO_4, $a_{Na_2SO_4} = 1$, and thus

$$a_{Na_2O} \rightleftharpoons \text{constant} \times a_{SO_3}^{-1} \quad \textbf{(3)}$$

At thermodynamic equilibrium, partial pressure calculates by FactSage are : $P(O_2)= 3.4*10^{-18}$ bar ; $P(SO_3)=9.0*10^{-19}$ bar. At 900°C, under these conditions, sodium sulphate transforms into Na_2S. Then, sodium sulfide freshly formed can be dissociate according to the reaction **(4)** :

$$Na_2S_{(s)} \rightleftharpoons H_2S_{(g)} + 2\ Na_{(g)} \quad \textbf{(4)}$$

At 900°C, under syngas atmosphere, the high partial pressure of $H_2S_{(g)}$ et $Na_{(g)}$ corroborate our theory ($P(H_2S) = 3.8*10^{-4}$ bar and $P(Na) = 8.4*10^{-5}$ bar).

However, it is probable that Na_2SO_4 decompose into Na_2S, then H_2S + Na, and at the same time, sodium sulphate reacts with CO to form sodium carbonate. This possibility could be confirmed by FactSage. In fact, when you put a x amount of Na_2SO_4 in syngas atmosphere excess, it forms at the thermodynamic equilibrium 0,9x of $Na_2S_{(s)}$ in addition to 0,1x of $Na_2CO_{3(l)}$.

This last one can then react with chromia to form a chromite according to reaction **(6)** by a basic fluxing model already reported in the literature [13-16].

$$Na_2SO_{4(l)} + CO_{2(g)} \rightleftharpoons Na_2CO_{3(l)} + SO_{3(g)} \quad \textbf{(5)}$$

$$Cr_2O_{3(s)} + Na_2CO_{3(l)} \rightleftharpoons 2\ NaCrO_{2(s)} + CO_{2(g)} \quad \textbf{(6)}$$

The fluxing mechanism [16] starts with the condensation of the salt on the alloy surface. Then, a cycle of subsequent chemical reactions takes place, initially attacking the protective oxide film and then depleting the chromium element from the substrate material. Due to the chromium depletion, oxidation of the base material accelerates and porous scale begins to form. After, catastrophic corrosions occur, with internal and external attacks. Rapp *et al.* [17] measured the oxide solubility in molten Na_2SO_4 as a function of the salt acidity. They suggested on the basis of their measurements that a negative gradient of the solubility of the protective oxide in the salt film at the oxide/salt interface should lead to the oxide dissolution at this interface and to the precipitation of a non-protective oxide away from the interface, where the solubility is lower. In this case fluxing arises only because of the local variation of sodium oxide activity and/or oxygen partial pressure across the salt film, without any necessity of sulphide-forming reactions. This mechanism can explain a self-sustaining process of dissolution of the protective oxide to maintain an accelerated corrosion attack [18].

However, in the present study, a different scenario is observed. Indeed after the first hours of oxidation, roughly corresponding of the time needed to evaporate the salt (Figure 3), the oxidation rate decreases and reaches a linear state similar to what can be observed without salt. Whereas nodule results of the catastrophic oxidation seem to disappear gradually, at the same time, chromium oxide comes back at the surface of the alloy. The development of nodule seems, in our case, to be reversible, as soon as salt is no longer present on the surface of the alloy. This observation is quite unusual regarding the literature of localized oxidation, most of the time irreversible and associated to the localized growth of iron-rich oxide [19,20]. Usually, breakaway is characterized by the failure of the protective oxide scales and the formation of iron nodules with accelerated kinetics. Several mechanisms leading to chromia scale failure on stainless steels appear in the literature. They are generally classed into three groups: failure by scale volatilization, pure chemical failure and mechanically induced failure [21]. Galerie *et al.* [20] report that iron oxide nodules suddenly appeared, first around the suspension hole and along sample edges, then on the main flat surfaces. For extended times, nodules overlapped and samples became entirely covered with iron-rich oxides. Galerie *et al.* conclude that when competition occurs between chromia and hematite on the steel

surface, hematite takes the leadership, leading to nodule formation and catastrophic oxidation. However, in our case, iron is thermodynamically not oxidable (Figure 9). Then, it is assumed that the presence of salt allows the oxidation of iron by altering the local oxygen chemical potential. In our study, catastrophic oxidation is also reversible from the moment where sodium sulphate disappears, and this phenomenon is certainly linked to the very low oxygen partial pressure.

Conclusion

At 900°C, under $CO/H_2/CO_2$ atmosphere with an oxygen partial pressure close to 10^{-18} bar, chromia-forming nickel based alloy, Haynes HR-120®, develops a chromium rich oxide protective scale. The presence of sodium sulphate induces a phenomenon of catastrophic oxidation. This one is characterized by an increase of the mass during the initial stage of oxidation associated with the presence of localized iron-rich oxide nodules. The development of iron oxide is probably linked to a fluxing mechanism of chromia in presence of salt. As soon as the salt is evaporated, a slower kinetic is observed and the nodules disappear. Haynes HR-120® in these specific conditions of oxidation could be considered as a self-healing material. The studies of the effect of other salts, in particular those thermodynamically stables in industrial conditions, and of regular additions of salt during oxidation, are planned to elucidate the corrosion resistance of this materials in simulated industrial conditions.

References

[1] F. Ropital, F. Bonnet, Mechanism of catalytic coke formation and some means to limit in refinery processes, Mater. Sci. Forum, 595-598 (2008) 681-688

[2] F. Bonnet, F. Ropital, Y. Berthier and P. Marcus, Filamentous carbon formation caused by catalytic metal particles from iron oxide, Mater. Corros. 54 (2003) 870-880

[3] I. Barin, Thermochemical Data of Pure Substance, 1ST Ed., VCH, New York, 1989

[4] R.E. Lobnig, H.P. Schmidt, K. Ennesen, H.J. Grabke, Oxid. Met. 37 (1992) 81-93

[5] N. Xu, D. Monceau, D. Young, J. Furtado, High temperature corrosion of cast heat resisting steels in $CO + CO_2$ gas mixtures, Corros. Sci. 50 (2008) 2398-2406

[6] T. Horita, H. Kishimoto, K. Yamaji, M.E. Brito, Y. Xiong, H. Yokokawa, Anomalous oxide scale formation of sodium containing gases for solid oxide fuel cell alloy interconnects, J. Power Sources, 193 (2009) 180-184

[7] H. Li, W. Chen, Stability of $MnCr_2O_4$ spinel and Cr_2O_3 in high temperature carbonaceous environments with varied oxygen partial pressure, Corros. Sci. 52 (2010) 2481-2488

[8] H. Li, Y. Zheng, L.W. Benum, M. Oballa, W. Chen, Carburization behaviour of Mn-Cr-O spinel in high temperature hydrocarbon cracking environment, Corros. Sci. 51 (2009) 2336-2341
[9] D.F. Susan, J.A. Van Den Avyle, S.L. Monroe, N.R. Sorensen, B.B. McKenzie, J.E. Christensen, J.R. Michael and C.A. Walker, The effects of pre-oxidation and alloy chemistry of austenitic stainless steels on glass/metal sealing, Oxid. Met. 73 (2010) 311-335
[10] J. Zurek, D.J. Young, E. Essuman, M. Haensel, H.J. Penkalla, L. Niewolak, W.J. Quadakkers, Growth and adherence of chromia based surface scales on Ni-base alloys in high- and low-p(O_2) gases, Mater. Sci. Eng. A, 447 (2008) 259-270
[11] A. Galerie, Y. Wouters, M. Caillet, The kinetic behaviour of metals in water vapour at high temperatures: Can general rules be proposed, Mater. Sci. Forum, 369-3 (2001) 231-238
[12] P. Promdirek, G. Lothongkhum, S. Chandra-ambhorn, Y. Wouters, A. Galerie, Behaviour of ferritic stainless steels subjected to dry biogas atmospheres at high temperatures Mater. Corr. 4 (2010) 62-68
[13] J.A. Goebel, F.S. Petit and G.W. Goward, Mechanisms for the hot corrosion of nickel-base alloys, Metall. Trans. 4 (1973) 261-278
[14] S. Zhao, X. Xie, G.D. Smith, The oxidation behavior of the new nickel-based superalloy Inconel 740 with and without Na_2SO_4 deposit, Surf. Coat. Technol. 185 (2004) 178-183
[15] G.M. Liu, F. Yu, J.H. Tian, J.H. Ma, Influence of the pre-oxidation on the hot corrosion of M38G superalloy in the mixture of Na_2SO_4-NaCl melts, Mater. Sci. Eng. A, 496 (2008) 40-44
[16] N.Eliaz, G. Shemesh, R.M. Latanision, Hot corrosion in gas turbine components, Eng. Fail. Ana. 9 (2002) 31-43
[17] R.A. Rapp and K.S Goto In: Proc. of Sympos. Fused Salts, ed. by J. Braunstein, and J.R. Selman (The Electrochem. Soc., Pennington, N.J., 1981) p.159
[18] J. Stringer, High temperature corrosion of superalloys, Mater. Sci. Technol. 3 (1987) 482-493
[19] A. Galerie, Y. Wouters, M. Pijolat, F. Valdivieso, M. Soustelle, T. Magnin, D. Delafosse, C. Bosch, B. Bayle, Mechanisms of corrosion and oxidation of metals and alloys, Adv. Eng. Mater. 3 (2001) 555-561
[20] A. Galerie, S. Henry, Y. Wouters, M. Mermoux, J.P. Petit, L. Antoni, Mechanisms of chromia scale failure during the course of 15-18Cr ferritic stainless steel oxidation in water vapour, Mater. High. Temp. 21 (2005) 105-112
[21] H.E. Evans, A.T. Donaldson, T.C. Gilmour, Mechanisms of breakaway oxidation and application to a chromia forming steel, Oxid. Met. 52 (1999) 379-402
[22] L. Tran, M. Anderson, D. Taylor, T.R. Allen, Corrosion of austenitic and ferritic-martensitic steels exposed to supercritical carbon dioxide, Corros. Sci. 53 (2011) 3273-3280

[23] F. Goutier, S. Valette, A. Vardelle, P. Lefort, Oxidation of stainless steel 304L in carbon dioxide, Corros. Sci. 52 (2010) 2403-2412

[24] F. Rouillard, C. Cabet, K. Wolski, M. Pijolat, Oxidation of a chromia-forming nickel base alloy at high temperature in mixed diluted CO/H_2O atmospheres, Corros. Sci. 51 (2009) 752-760

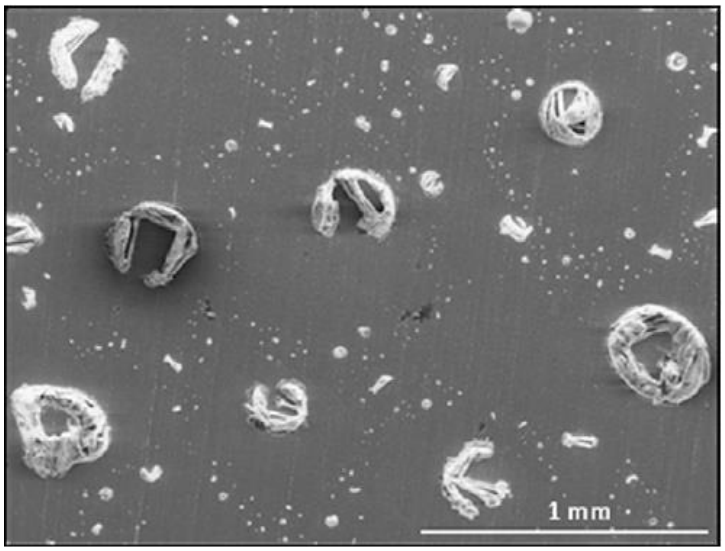

Fig. 1: SEM surface view of the salt particles covering specimens after the heating step at 150°C

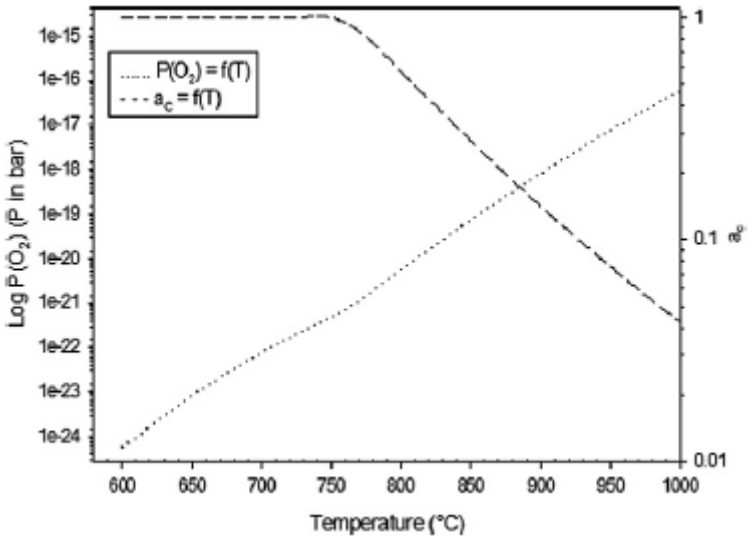

Fig. 2: Oxygen and carbon activity of the syngas atmosphere as a function of temperature [FactSage, SGTE 2009]

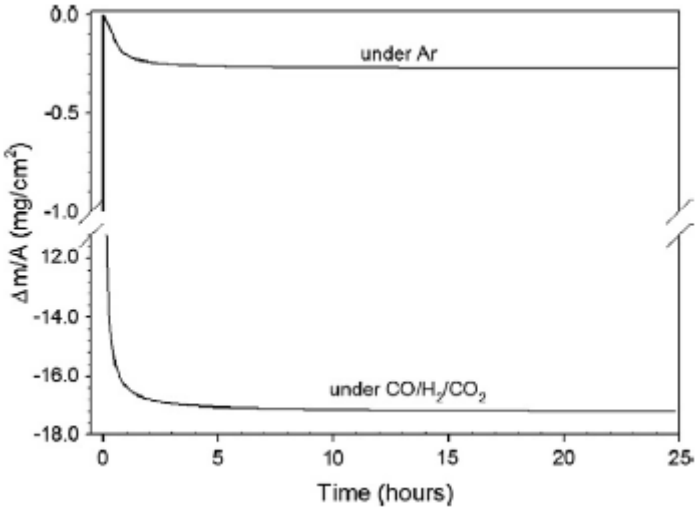

Fig. 3: Mass losses due to Na_2SO_4 evaporation according atmospheres (T = 900°C, initial amount of salt: 34 mg)

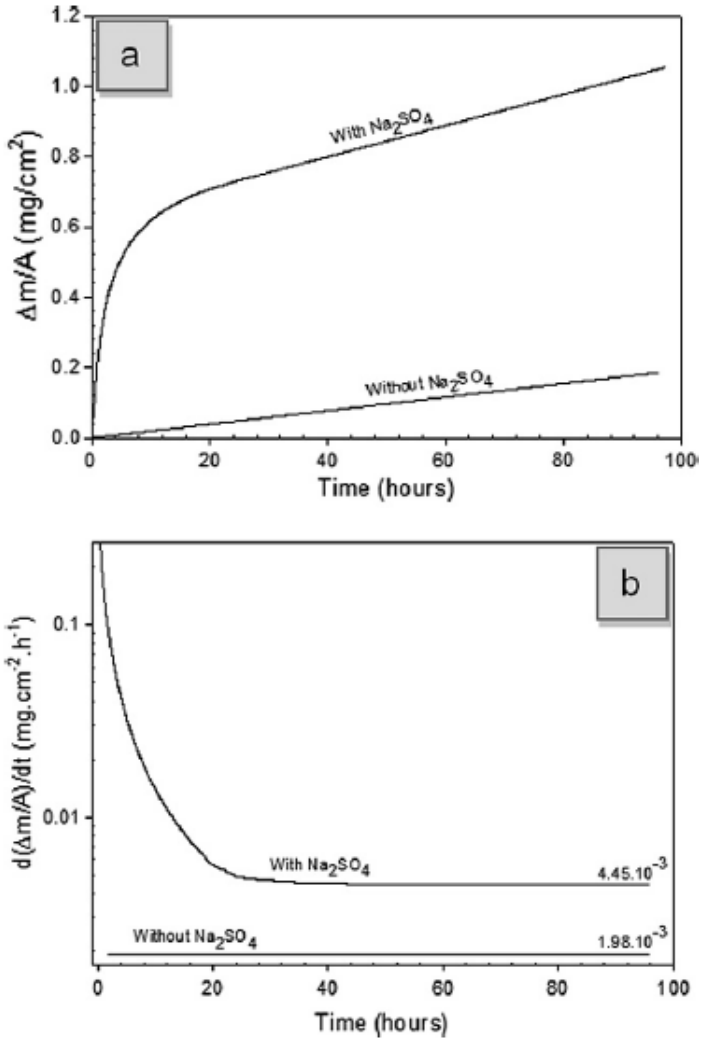

Fig. 4: (a): TGA of HR-120 with and without salt at 900°C in $CO/H_2/CO_2$ (45/45/10 %vol.), (b): derivative of mass gain with time

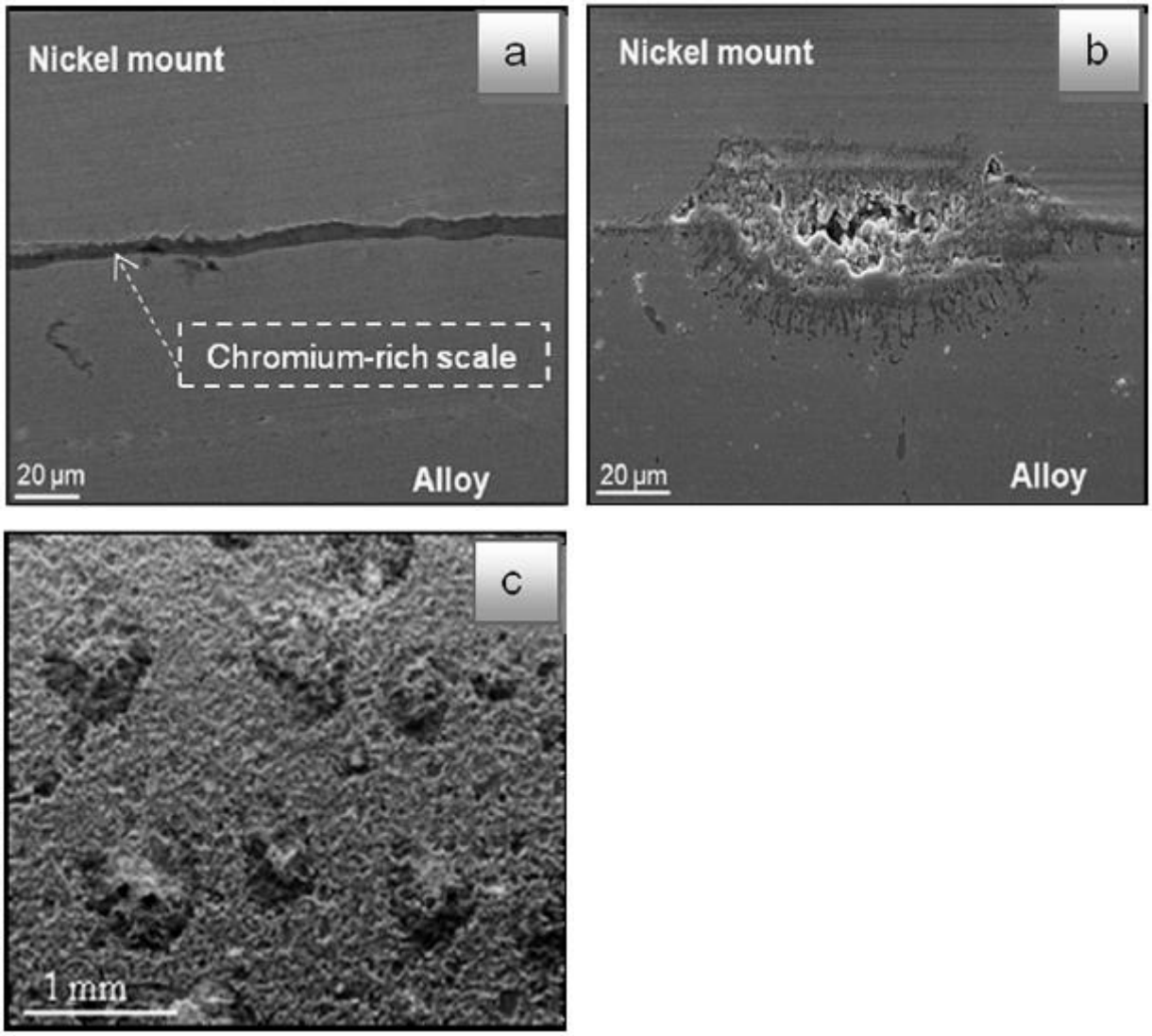

Fig. 5: SEM cross-section of HR-120 tested for 96 h at 900°C (secondary electrons) (a) without and (b) with sodium sulphate, (c) SEM surface view of nodules with sodium sulphate (secondary electrons)

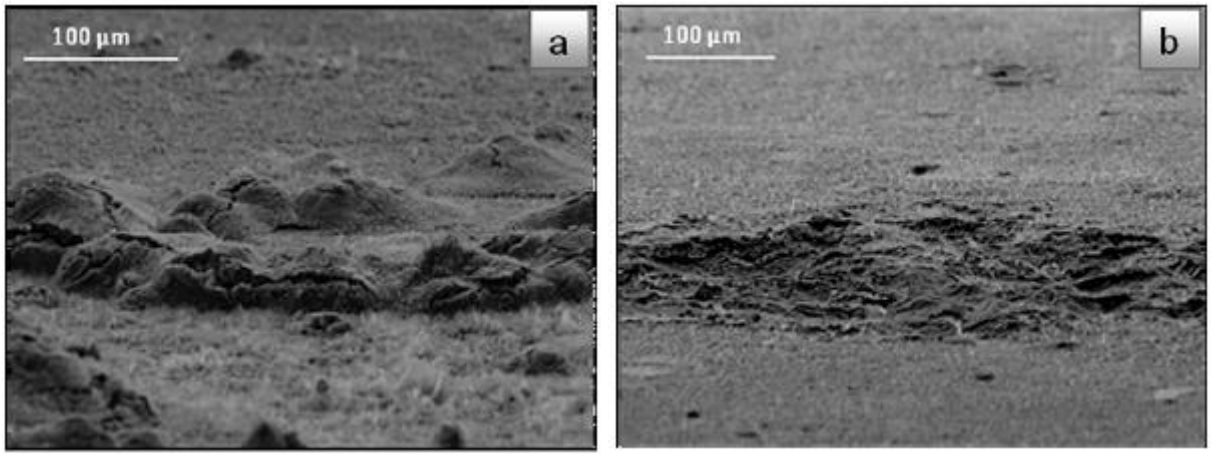

Fig. 6: Surface SEM observations (80° tilted) of the HR-120 treated with sodium sulphate at 900°C (secondary electrons) (a) 1h and (b) 96 h

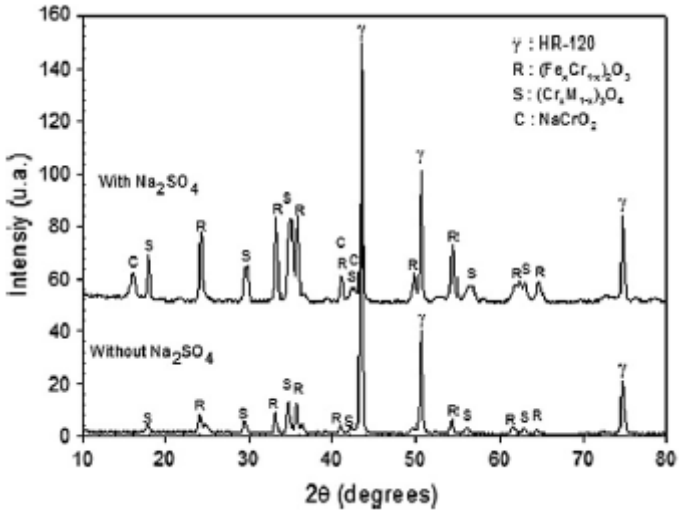

Fig. 7: XRD of HR-120 after 96 h at 900 °C with and without sodium sulphate

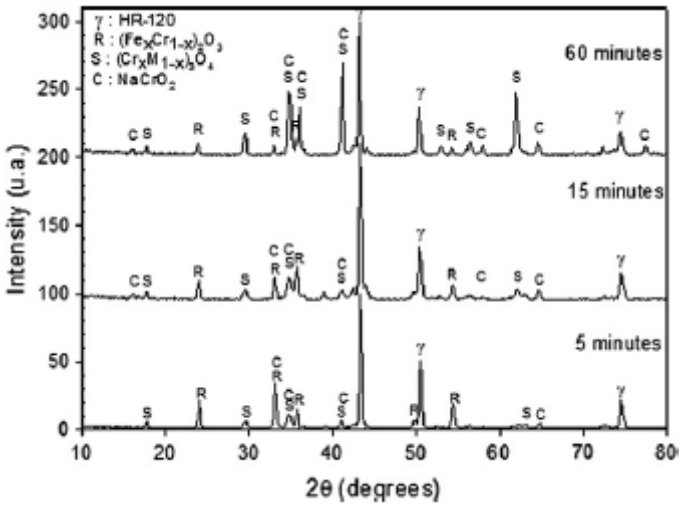

Fig. 8: XRD of HR-120 with sodium sulphate at 900°C after short time of exposition

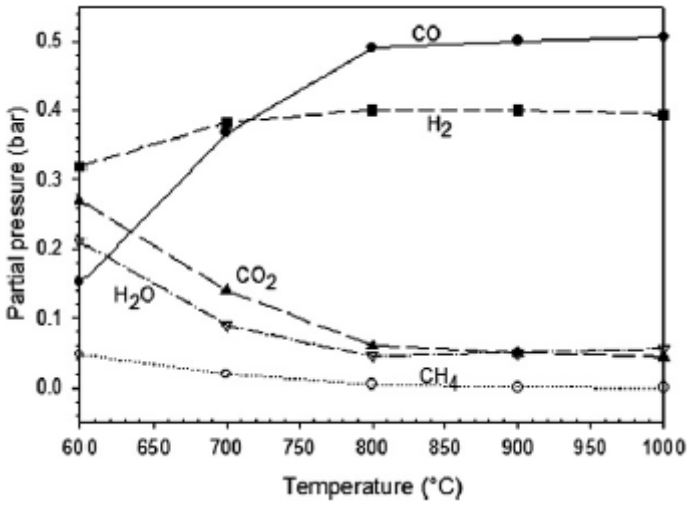

Fig. 9: Equilibrium composition of the syngas as a function of temperature. Initial mixture composition: 45CO, 45H_2, 10CO_2 [FactSage, SGTE 2009]

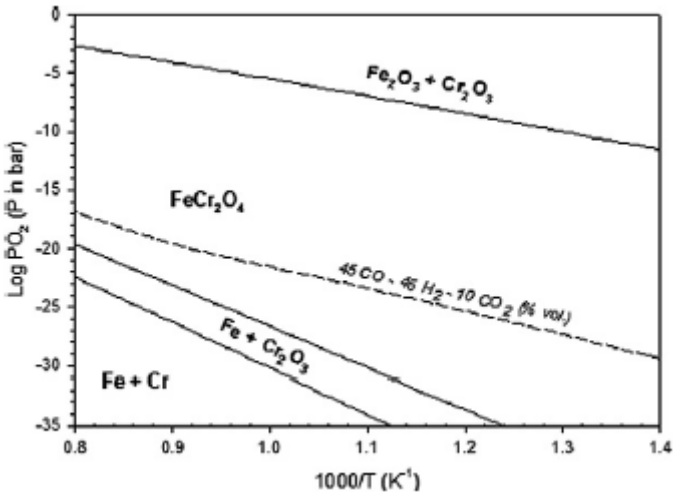

Fig. 10: Stability diagram of oxides in the iron-chromium-oxygen system [FactSage, SGTE 2009]

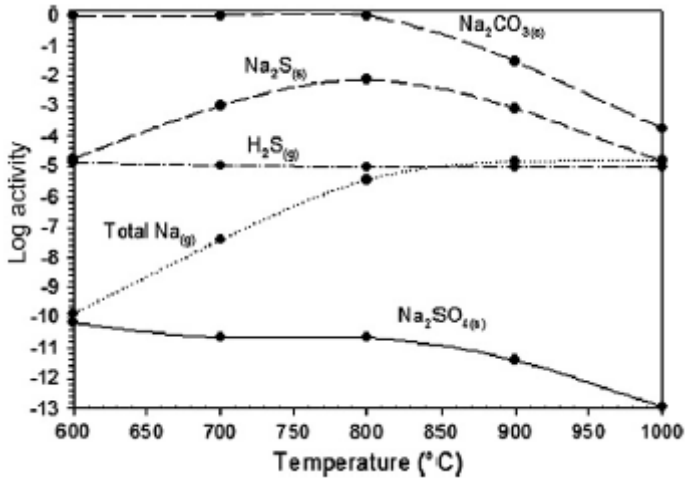

Fig. 11: Equilibrium situation for the major constituents. Inputs : 100 mol gas mixture + 10^{-3} mol $Na_2SO_{4(s)}$ [FactSage, SGTE 2009]

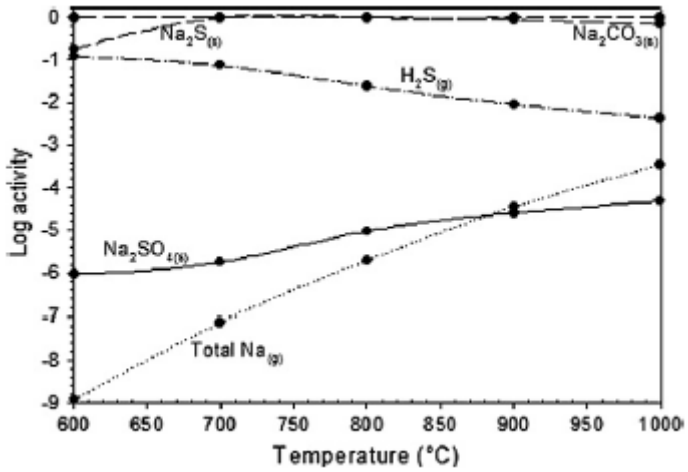

Fig. 12: Equilibrium situation for the major constituents. Inputs : 100 mol gas mixture + 10 mol $Na_2SO_{4(s)}$ [FactSage, SGTE 2009]

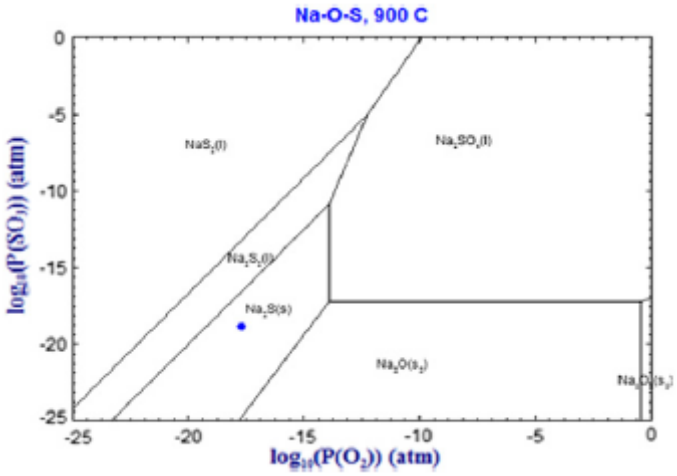

Fig. 13: Phase stability diagram for the Na-O-S system at 900°C [FactSage, SGTE 2009]

Table 1: Chemical composition of HR-120 (wt%)

Fe	Ni	Cr	Co	Mo	W	Nb	Mn	Si	Al	C	B
34.34	37.97	25.17	0.11	0.34	0.08	0.61	0.77	0.41	0.06	0.05	0.002